



OPEN

Interfacial stabilization for epitaxial CuCrO₂ delafossites

Jong Mok Ok^{1,3}, Sangmoon Yoon^{1,3}, Andrew R. Lupini², Panchapakesan Ganesh², Matthew F. Chisholm² & Ho Nyung Lee^{1✉}

ABO₂ delafossites are fascinating materials that exhibit a wide range of physical properties, including giant Rashba spin splitting and anomalous Hall effects, because of their characteristic layered structures composed of noble metal *A* and strongly correlated *BO₂* sublayers. However, thin film synthesis is known to be extremely challenging owing to their low symmetry rhombohedral structures, which limit the selection of substrates for thin film epitaxy. Hexagonal lattices, such as those provided by Al₂O₃(0001) and (111) oriented cubic perovskites, are promising candidates for epitaxy of delafossites. However, the formation of twin domains and impurity phases is hard to suppress, and the nucleation and growth mechanisms thereon have not been studied for the growth of epitaxial delafossites. In this study, we report the epitaxial stabilization of a new interfacial phase formed during pulsed-laser epitaxy of (0001)-oriented CuCrO₂ epitaxial thin films on Al₂O₃ substrates. Through a combined study using scanning transmission electron microscopy/electron-energy loss spectroscopy and density functional theory calculations, we report that the nucleation of a thermodynamically stable, atomically thick CuCr_{1-x}Al_xO₂ interfacial layer is the critical element for the epitaxy of CuCrO₂ delafossites on Al₂O₃ substrates. This finding provides key insights into the thermodynamic mechanism for the nucleation of intermixing-induced buffer layers that can be used for the growth of other noble-metal-based delafossites, which are known to be challenging due to the difficulty in initial nucleation.

ABO₂ delafossite oxides have attracted considerable interest because of their fascinating properties that depend on the choice of *A* and *B* site elements^{1–3}. Metallic delafossites, especially PdCoO₂ and PdCrO₂, exhibit very high conductivity on the order of 10^{–8} Ω cm with an extremely long mean free path of *l_m* ~ 20 μm at low temperatures^{4,5}. While the high conductivity and the large spin–orbit coupling associated with huge Rashba splitting⁶ make such metallic delafossites promising candidates for future spintronic devices, their synthesis in thin film forms has not been established. There have been several attempts to grow metallic delafossite thin films, and Pd-based delafossites were recently grown by pulsed laser epitaxy (PLE)^{7–9} and molecular beam epitaxy (MBE)^{10,11}. The quality and performance of thin films, however, are not as good as those of single crystals, thus further improvements are needed. The major problem that needs to be overcome is the poor structural quality due to the formation of twin domains and impurity phases^{7–11}, which mainly originate from the initial nucleation and structural dissimilarity between the film and substrate. To achieve high quality thin films, therefore, not only is an isostructural substrate or buffer layer with similar lattice parameters needed, but also a deeper understanding on the nucleation and growth mechanisms.

Among various delafossite compounds, Cu-based delafossites are good candidates for resolving the major problems for two reasons. First, the Cu-based delafossites could be utilized as isostructural substrates or buffer layers because of their high resistivity and small lattice mismatch with Pd-based delafossites^{1–3}. Second, Cu-based delafossites are known to be readily grown as thin films^{12–18}. For example, CuCrO₂ thin films grown on Al₂O₃ substrates are known to be one of the best delafossite thin films with high crystallinity and no impurity phase formation^{12–18}. Thus, understanding their growth and nucleation mechanisms can provide guidance on how to grow other delafossite films. Furthermore, we have recently found that deposition of a CuCrO₂ monolayer before the growth of the PdCrO₂ thin film significantly reduced the appearance of impurity phases⁹, whereas the formation of a large amount of Cr₂O₃ impurity was inevitable for the direct growth of PdCrO₂ without the buffer layer⁹. In the context of lattice mismatch (δ (%) = $(a_s - a_f)/a_s \times 100\%$, where *a_s* and *a_f* are the lattice parameters of the substrate and film, respectively), the role of CuCrO₂ buffer layer is quite puzzling, because the lattice mismatch of $\delta = 7.2\%$ between CuCrO₂ and Al₂O₃ is larger than that ($\delta = 5.9\%$) of PdCrO₂ on Al₂O₃. Thus, the growth of

¹Materials Science and Technology Division, Oak Ridge National Laboratory, Oak Ridge, TN 37831, USA. ²Center for Nanophase Materials Sciences, Oak Ridge National Laboratory, Oak Ridge, TN 37831, USA. ³These authors contributed equally: Jong Mok Ok and Sangmoon Yoon. ✉email: hnlee@ornl.gov

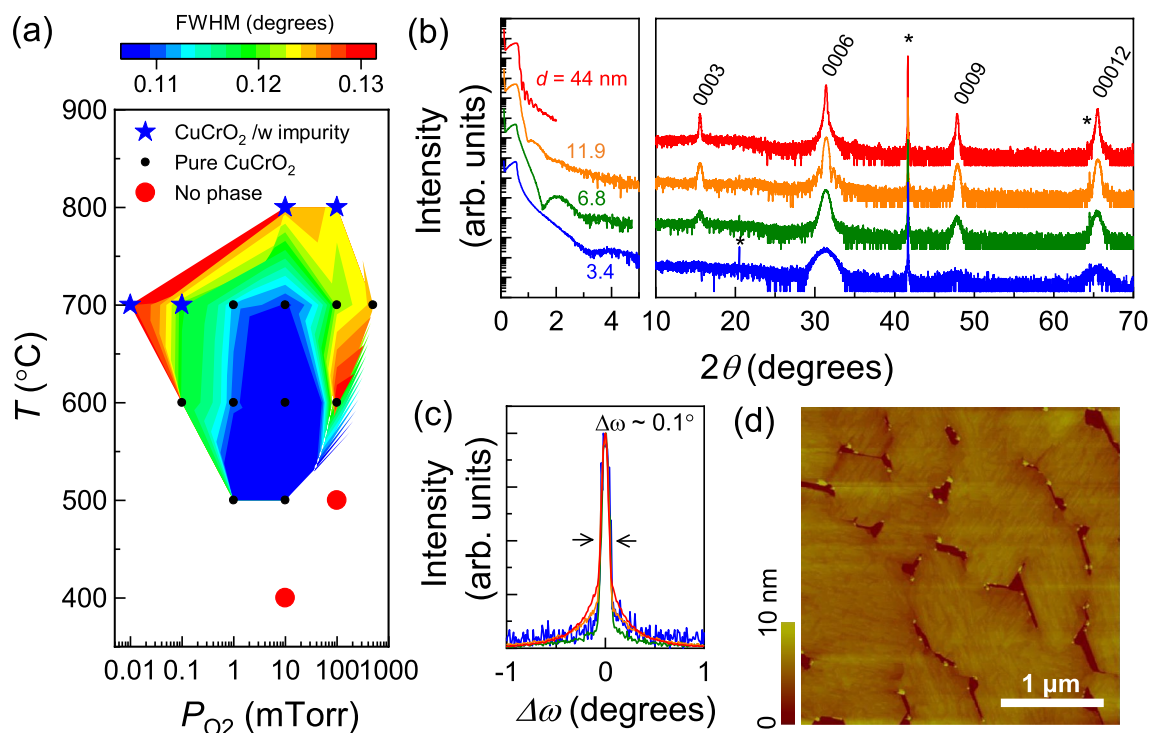


Figure 1. (a) Contour plot of full-width at half-maximum (FWHM) of the CuCrO₂ 0006 peak as a function of oxygen pressure and growth temperature. The blue area corresponds to the optimum growth window, in which CuCrO₂ thin films exhibit low FWHM values ($<0.1^\circ$). (b) X-ray reflectivity and X-ray diffraction 2θ - θ patterns of CuCrO₂ thin films with different film thicknesses grown under the optimum growth condition, and (c) their FWHM of the CuCrO₂ 0006 peak, exhibiting FWHM $\sim 0.1^\circ$. (d) Atomic force microscopy (AFM) image of a CuCrO₂ thin film (10 nm in thickness).

high-quality CuCrO₂ thin films cannot be simply understood from conventional thin film growth mechanisms; therefore, a direct observation of the atomic and electronic structure of the CuCrO₂/Al₂O₃ interface is required to reveal the underlying reason for how the epitaxy of CuCrO₂ on Al₂O₃ is accomplished despite the relatively large lattice mismatch.

In this study, we grew high-quality CuCrO₂ thin films by systematically tuning the growth conditions, including the growth temperature (T) and oxygen partial pressure (P_{O_2}). Our films revealed a high crystallinity, smooth surface, and reasonably high resistivity. Using these high-quality CuCrO₂ thin films, we studied the interface microstructure to understand the nucleation and growth behavior of CuCrO₂ using scanning transmission electron microscopy (STEM)/electron energy loss spectroscopy (EELS) and density functional theory (DFT) calculations. We have found that atomic-level interfacial intermixing between Al and Cr atoms within the atomic-layer thick substrate surface plays a critical role in stabilizing the nucleation of the CuCrO₂ delafossite phase. The initial intermixing-induced nucleation seems important to both reduce the most stable impurity phase, Cr₂O₃, and to stabilize the high-quality CuCrO₂ phase.

To grow CuCrO₂ thin films with high crystallinity, we mapped out the optimal growth condition for CuCrO₂ thin films on Al₂O₃ (0001) substrates by varying the temperature and oxygen partial pressure using a single-phase CuCrO₂ target (see Figure S1 in Supplementary Information). Figures S1a,b show X-ray diffraction (XRD) 2θ - θ scans for CuCrO₂ films grown under different T and P_{O_2} conditions. The CuCrO₂ phase could be stabilized under a wide range of growth conditions, but an impurity phase was observed under both low P_{O_2} (<0.01 mTorr) and high T ($>800^\circ\text{C}$) growth conditions. Figure 1a summarizes results for CuCrO₂ films grown at different T and P_{O_2} . The contour plot indicates rocking curve full width at half maximum (FWHM) values of the 0006 CuCrO₂ peak, and the symbols indicate whether the film is single-phase (black circles) or has impurity phases (blue stars). This result indicates that the growth window for the epitaxy of CuCrO₂ films is relatively wide ($500 < T < 800^\circ\text{C}$ and $0.01 < P_{O_2} < 500$ mT). We found the best quality films were grown at $T = 650^\circ\text{C}$ and $P_{O_2} = 10$ mTorr.

Figure 1b shows X-ray reflectivity (XRR) and XRD patterns of CuCrO₂ thin films with different thicknesses ($d = 3.1$ – 44 nm) grown on Al₂O₃ (0001) at the optimum condition ($T = 650^\circ\text{C}$ and $P_{O_2} = 10$ mTorr). XRR results of all films show clear interference fringes, indicating smooth surfaces of CuCrO₂ thin films. All of the film peaks in the XRD patterns correspond to the delafossite 0003n peaks. The width of the CuCrO₂ 0003n peaks become broader with decreasing film thickness, as expected from the Laue function. As shown in Fig. 1c, the rocking curve FWHM values for the 0006 peak of CuCrO₂ films are $\sim 0.1^\circ$, which is smaller than those in previous reports. Figure 1d shows an atomic-force microscopy (AFM) image of a CuCrO₂ thin film surface, showing a triangular shaped grain boundary (we note that such a grain boundary can act as a scattering center in the carrier relaxation process, yielding a higher resistivity than materials without such disorder). The root mean

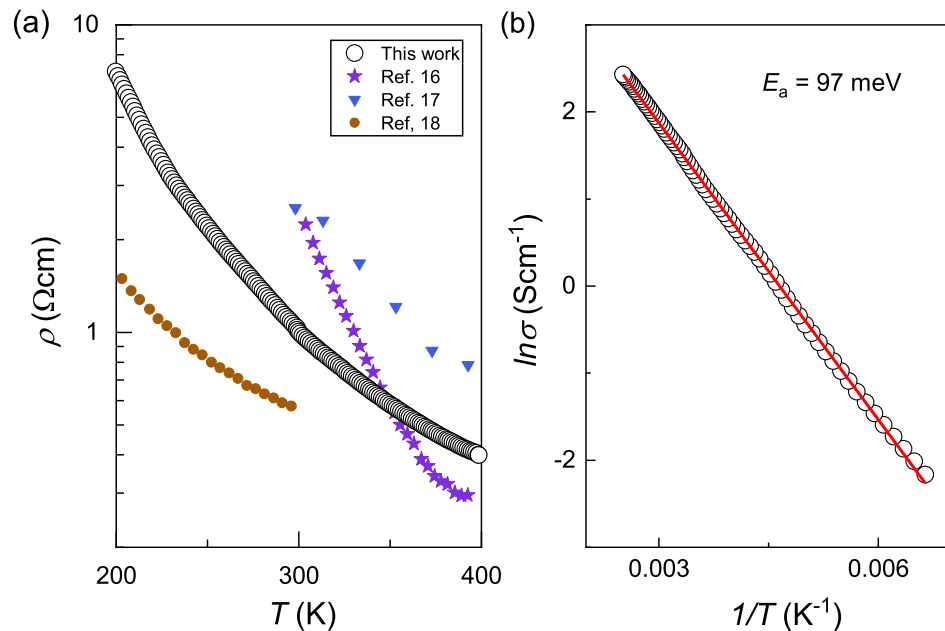


Figure 2. (a) Temperature dependence of *dc* resistivity of a CuCrO₂ thin film, which is compared with films grown by various methods, including PLE¹⁶, magnetron sputtering¹⁷, and atomic layer deposition¹⁸. (b) $\ln \sigma$ vs. $1/T$ plots for CuCrO₂ thin film, showing the activation energy of 97 meV.

square (RSM) roughness of our film was estimated to be 1.58 nm over a $3 \times 3 \mu\text{m}^2$ range. The RSM roughness of a structural domain was only 0.25 nm, which is much smaller than that from spin-coated^{12,13} and MBE-grown films¹⁴ (RSM = ~3–50 nm). The RSM value is even smaller than that from previously PLE grown CuCrO₂ thin films (RSM = ~1 nm)¹⁵. Figure 2a shows the temperature dependence of 4-probe *dc* resistivity for a CuCrO₂ thin film (11.5 nm), which exhibits semiconducting behavior ($d\rho/dT < 0$). The thermal activation energy of charge carriers was ~97 meV as shown in Fig. 2b, which is consistent with previous reports from thin film samples^{16–18}. Overall, the epitaxial growth of high-quality CuCrO₂ thin films is particularly notable if we consider that the growth of delafossite thin films without impurity phases is a big challenge in many other compounds, e.g. PdCrO₂, PdCoO₂, and PtCoO₂.

Figure 3a shows a high-angle annular dark field (HAADF) STEM image of a CuCrO₂ thin film grown on an Al₂O₃ (0001) substrate seen along the $[\bar{1}100]$ zone axis. The brightest and second brightest features in this image indicate Cu and Cr atomic columns, respectively. Note the HAADF STEM provides scattering intensities that are approximately proportional to the square of the atomic number. Thus, the lightest element, O, is not visible in this HAADF STEM image. The HAADF image confirms that the CuCrO₂ thin film is epitaxially grown on the Al₂O₃ (0001) substrate. The atomic structure at the interface, shown in Fig. 3a,b, exhibits several interesting aspects. First, the growth of the CuCrO₂ thin film initiates with the CrO₂ sublayer, followed by the Cu sublayer. Second, the top one or two layers of the Al₂O₃ substrate exhibit a brighter intensity than the bulk layers of the substrate. In this study, a monolayer (ML) of each material was defined to satisfy stoichiometry. That is, the MLs for CuCrO₂ thin film were composed of a set of Cu and CrO₂ sublayers (thickness: 0.57 nm) and for Al₂O₃ substrate in the (0001) direction as a single Al₂O₃ layer (thickness: 0.22 nm), which are illustrated in Fig. 4b. Thus the increased intensity implies that some atomic-level interfacial intermixing occurred during the initial stage of film growth. Although it was not identified previously, these interfacial features were also similarly observed in a PdCrO₂ thin film grown on a CuCrO₂-buffered Al₂O₃ (0001) substrate⁹. In addition, the HAADF STEM image shows that stacking faults exist in the delafossite CuCrO₂ thin film, denoted by black lines on the left side of Fig. 3a. Such stacking faults were frequently observed in previous PLE or MBE grown delafossite films^{9,10}. The presence of these stacking faults indicates that their formation energies are relatively small in this delafossite film. Further studies will be required to understand the influence of stacking faults on the optical and transport properties of delafossite materials.

To systematically understand the interface structure and the nucleation of epitaxial growth of CuCrO₂ thin films, EELS spectrum imaging was performed across the CuCrO₂/Al₂O₃ interface as shown in Fig. 3c–g. Previous studies have shown that the direct interpretation of interface structure can be achieved only under very thin specimen conditions (ideally less than approximately 20 nm)^{19,20}. Otherwise, complex propagation effects, which include beam broadening, cross-talk, and dechanneling, result in the potential misinterpretation of interface structure^{21,22}. For this study, we selected a thin region of a specimen for atomic-scale quantification of the interface structure. Thickness measurements across the interface using low-loss EELS spectra are shown in Figure S2 of the Supplementary Information. We confirmed by the 2D spectrum line profile that core-loss excitations are sensitive to the individual atomic planes (see Figure S3 in Supplementary Information). The O–*K* and Cr–*L*_{2,3} edge signals dropped to almost zero at the Cu sublayers, as did the Cu–*L*_{2,3} edge at the CrO₂ sublayers. Figure 3c shows a HAADF STEM image of the CuCrO₂/Al₂O₃ interface, which is simultaneously acquired during EELS

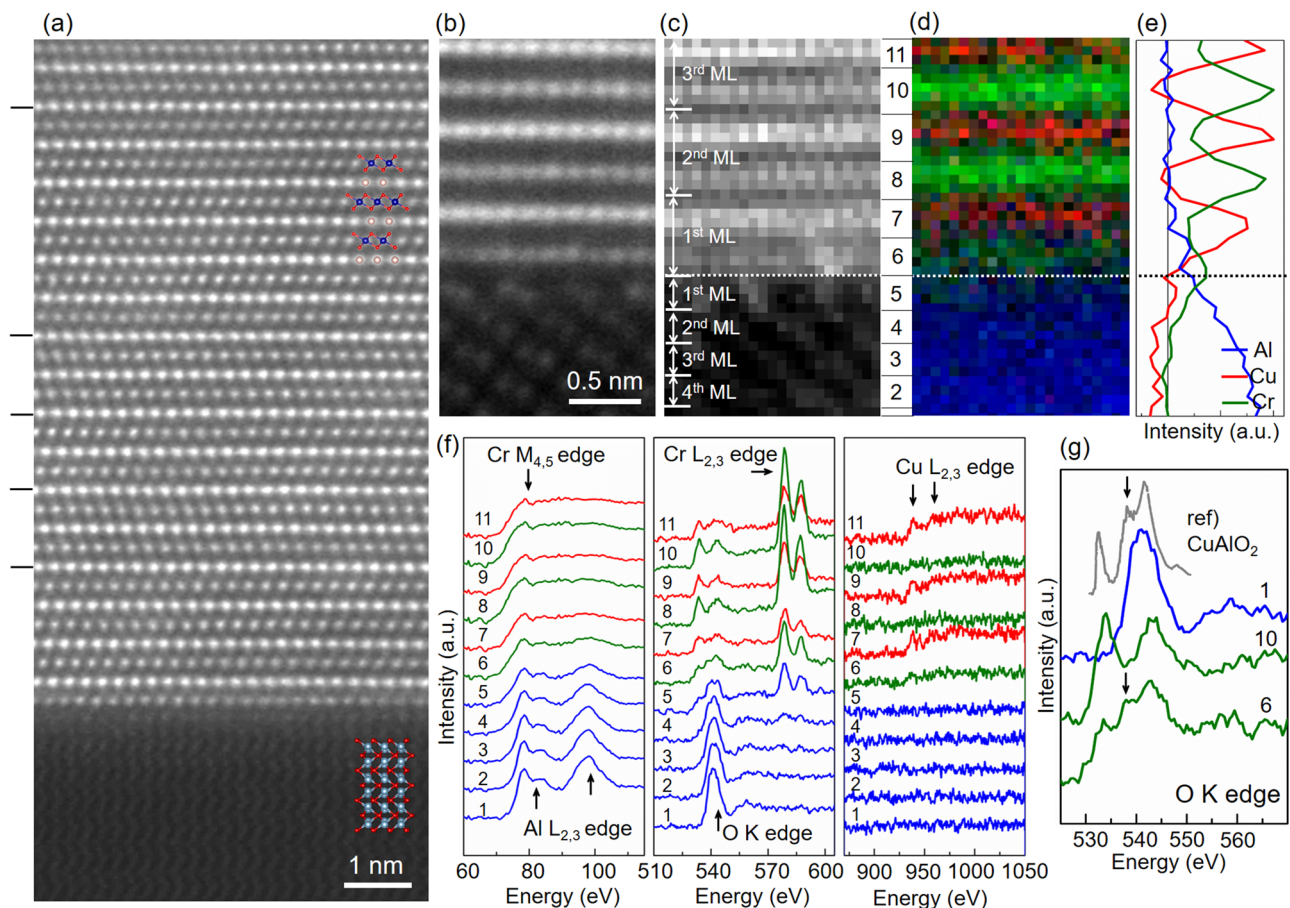


Figure 3. (a, b) High-angle annular dark field (HAADF) scanning transmission electron microscopy (STEM) image of a CuCrO₂ thin film grown on an Al₂O₃ (0001) substrate seen along the (a) [1100] and (b) [1000] zone axis. (c)–(f) Electron energy loss spectroscopy (EELS) spectrum imaging of the CuCrO₂/Al₂O₃ interface seen along the [1000] zone axis. The monolayers (MLs) for CuCrO₂ thin film and Al₂O₃ substrate in the (0001) direction were defined as a set of Cu and CrO₂ sublayers and a single Al₂O₃ layer, respectively. (c) Simultaneously acquired HAADF-STEM image. (d) Color-coded composite elemental map with Al in blue, Cr in green, and Cu in red. (e) Integrated line profile of Al, Cr, and Cu signals in (d) across the interface. The dotted lines in (c)–(e) indicate the position of the CuCrO₂/Al₂O₃ interface. (f) Layer-resolved integrated EELS spectra of Al-*L*_{2,3}, Cr-*M*_{4,5}, O-*K*, Cr-*L*_{2,3}, and Cu-*L*_{2,3} edges. The position of the atomic layer corresponding to each EELS spectrum is indicated by the numerical index between (c) and (d). (g) EELS O-*K* edge spectra of the Al₂O₃ substrate, CuCrO₂ thin film, and CuCrO₂/Al₂O₃ interface with an X-ray absorption spectroscopy (XAS) O-*K* edge reference spectrum of CuAlO₂³⁰. It is worth noting that no discernible vacancy-related features could be detected from the integrated line-profile spectra.

spectrum imaging. Figure 3d,e show a color-encoded elemental map and an elemental line profile, respectively, across the interface with Al in blue, Cr in green, and Cu in red. Figure 3f shows layer-resolved integrated EELS spectra of Al-*L*_{2,3}, Cr-*M*_{4,5}, O-*K*, Cr-*L*_{2,3}, and Cu-*L*_{2,3} edges. Figure 3g highlights a collection of O-*K* edge spectra of the Al₂O₃ substrate, CuCrO₂ thin film, and CuCrO₂/Al₂O₃ interface. The position of the atomic layer corresponding to each spectrum in Fig. 3f,g is denoted in between Fig. 3c,d. For elemental mapping and the line profile, the second peak of Al-*L*_{2,3} edge, Cr-*L*_{2,3} edge, and Cu-*L*_{2,3} edge signals in Fig. 3f were used; because the first peak of Al-*L*_{2,3} edge overlaps with the Cr-*M*_{4,5} edge signal. To minimize specimen damage due to electron beam irradiation, EELS spectrum imaging was performed using a low-current electron probe with a short exposure time (0.01 s per pixel).

Even in the thinnest specimen section, both Cr and Al elements are clearly detected across the interface as shown in Fig. 3d,e, suggesting interlayer mixing occurred at the interface during the film growth. We note that the plume energy in PLE growth is quite high (1–100 eV)²³, exceeding the surface bonding energy of substrate materials (typically on the order of 1 eV). Thus, the growth species can easily penetrate into the substrate surface^{23,24}, resulting in intermixing of elements especially under high vacuum conditions. Interestingly, the concentration of Cr was significantly reduced only for the first ML of the CuCrO₂ thin film. The stoichiometry of the CuCrO₂ layer appears to be fully recovered from the second ML of the film, indicating that the interfacial inter-layer-mixing in the thin film largely occurred within one ML. The Cr-*L*_{2,3} edge spectra in Fig. 3f further confirmed that Cr atoms penetrated up to two MLs below the interface, and the oxidation state of Cr ions was maintained as Cr³⁺ even in the Al₂O₃ substrate side (the shape and energy of the Cr-*L*₃ edge do not change across the interface^{25,26}).

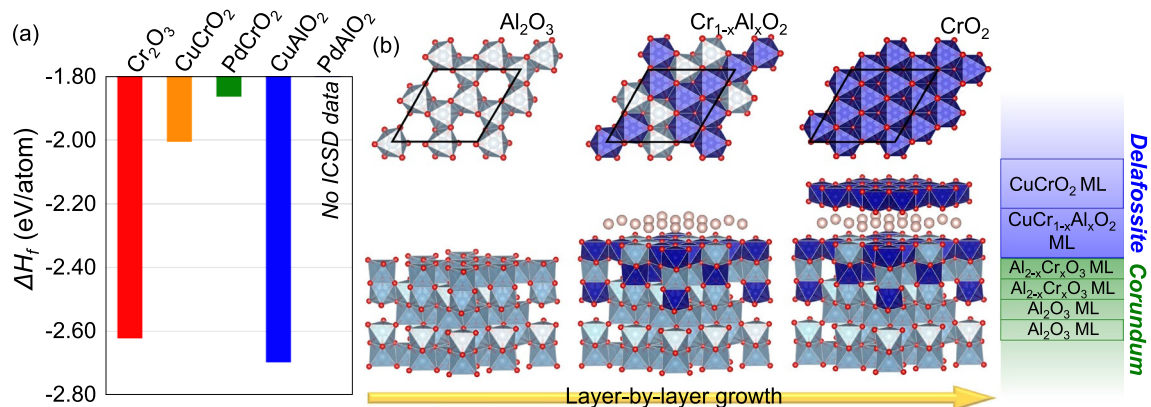


Figure 4. (a) Formation enthalpy (ΔH_f) of Cr-based delafossite-related materials estimated by DFT-based fitted elemental-phase reference energies (FERE) method. Structural information of PdAlO_2 with delafossite symmetry ($R\bar{3}m$ or $P6_3/mmc$ space group) was considered to compare with other delafossites, but the information is absent in the Inorganic Crystal Structure Database (ICSD). (b) Schematics of top and cross-sectional views of a $\text{CuCrO}_2/\text{Al}_2\text{O}_3$ heterostructure, describing the layer-by-layer growth of a CuCrO_2 thin film on an Al_2O_3 substrate with an atomic-layer thick $\text{CuCr}_{1-x}\text{Al}_x\text{O}_2$ nucleation layer. The top view of the top-most surface layer is illustrated on each schematic; Cu atoms are not included in the top view of the surface layer for clear visualization of symmetry matching between delafossite and corundum structures. The MLs of CuCrO_2 and Al_2O_3 are denoted by blue- and green-outlined rectangles on the right side of (b), respectively.

Meanwhile, the $\text{Cu}-L_{2,3}$ edge was not detected on the substrate side, verifying that Al atoms were intermixed with the B -site Cr atoms not Cu atoms. In general, the $\text{O}-K$ edge in transition metal oxides has been used for the investigation of the individual electronic structure of materials, since the $1s$ core states have a relatively small exchange interaction with the final states, resulting in no visible multiplet effects^{27–29}. The $\text{O}-K$ edge spectra profile across the interface confirms that one ML above the interface and two MLs below the interface exhibits the characteristic electronic structures from those of the CuCrO_2 thin film and Al_2O_3 substrate, respectively. More interestingly, the $\text{O}-K$ edge of the first ML of the CuCrO_2 thin film (spectrum #6) revealed the same spectral signature as that of the CuAlO_2 delafossite, which is shown in Fig. 3g. The overall shape of the $\text{O}-K$ edge of the first ML is similar to that of CuAlO_2 ³⁰, and, in particular, the peak indicated by the black arrow, which cannot be explained by the $\text{O}-K$ edge spectra of the existing CuCrO_2 and Al_2O_3 , only appears in the $\text{O}-K$ edge of the first ML. The in-depth analysis of EELS spectral images strongly suggests that the interfacial intermixing, which occurred during the initial stage of the epitaxial growth, creates an atomically thin ML of $\text{CuCr}_{1-x}\text{Al}_x\text{O}_2$ alloy.

To evaluate the thermodynamic stability of delafossites compared to the Cr_2O_3 impurity phase, the formation enthalpy (ΔH_f) was calculated using the DFT-based fitted elemental-phase reference energies (FERE) method³¹. As shown in Fig. 4a, ΔH_f of Cr-based delafossites, including CuCrO_2 and PdCrO_2 , were far greater than that of Cr_2O_3 , accounting for the formation of Cr_2O_3 impurities. Interestingly, CuAlO_2 was found to be much more stable than CuCrO_2 and even more stable than Cr_2O_3 ; 0.08 eV/atom lower than that for Cr_2O_3 . These numerical results suggest that the substitution of Al atoms for Cr atoms in CuCrO_2 will lower its formation enthalpy. This thermodynamic consideration explains the formation of the $\text{CuCr}_{1-x}\text{Al}_x\text{O}_2$ interfacial ML we observed in our STEM-EELS investigations. In addition, the interfacial mixing helps to reduce the epitaxial strain as the lattice constant of $\text{CuCr}_{1-x}\text{Al}_x\text{O}_2$ is closer to the Al_2O_3 substrate than for pure CuCrO_2 . It is worth noting that the formation of PdAlO_2 has not been experimentally reported so far, suggesting that the substitution of Al atoms for Cr atoms to form the equivalent interfacial $\text{PdCr}_{1-x}\text{Al}_x\text{O}_2$ for the growth of epitaxial PdCrO_2 on Al_2O_3 is unlikely.

The STEM-EELS and DFT results provide direct insights into the nucleation of epitaxial growth of CuCrO_2 thin films and the critical role of a CuCrO_2 buffer layer for the epitaxy of delafossites. First, inter-layer-mixing was observed at the interface, but not further into the film, indicating that it happens at the initial nucleation step of the epitaxial growth. At the initial nucleation stage, Cr atoms will penetrate into the sub-surface-layers of the Al_2O_3 substrate and, as an exchange, Al atoms will out-diffuse to the surface. Second, the free Al atoms at the surface will act to stabilize the nucleation of CuCrO_2 delafossite thin films. Without these Al atoms, the Cr_2O_3 will be the most stable phase at the nucleation step, disturbing the formation of the delafossite phase. Third, the homogenous and stable nucleation, with the delafossite symmetry provided by $\text{CuCr}_{1-x}\text{Al}_x\text{O}_2$, will enable the high-quality growth of CuCrO_2 thin films. The growth process understood here is summarized in Fig. 4b. In a previous study, we reported that the use of a one-ML-thick CuCrO_2 buffer layer significantly suppressed the formation of Cr_2O_3 impurities in the epitaxy of PdCrO_2 thin films⁹. It was quite puzzling because the lattice mismatch of the $\text{CuCrO}_2/\text{Al}_2\text{O}_3$ interface ($\delta = 7.2\%$) is much larger than that of the $\text{PdCrO}_2/\text{Al}_2\text{O}_3$ interface ($\delta = 5.9\%$), which is counter intuitive. Our discovery of the formation of the $\text{CuCr}_{1-x}\text{Al}_x\text{O}_2$ delafossite at the $\text{CuCrO}_2/\text{Al}_2\text{O}_3$ interface now explains the role of the CuCrO_2 buffer layer in the growth of the PdCrO_2 thin films. The deposition of CuCrO_2 buffer layer will induce the homogenous and stable nucleation with delafossite symmetry, which cannot be achieved from the direct deposition of PdCrO_2 layers. Note again that the preferential nucleation by Al substitution only occurs for Cu-based delafossites, not for Pd-based delafossites; the substitution of Al atoms for Cr atoms acts to decompose PdCrO_2 delafossite films.

In summary, we have grown high quality CuCrO₂ thin films by pulsed laser epitaxy. Compared with CuCrO₂ thin films grown by other methods, PLE grown films show better quality in terms of crystallinity and surface roughness. The successful growth was possible owing to the non-equilibrium energetic process of PLE growth. The intermixing-induced alloying of the Al and Cr atoms was found to play a crucial role in stabilizing the nucleation of CuCrO₂ delafossite phase and in reducing the most stable impurity phase Cr₂O₃ often found in other delafossites. We believe a similar consideration can be also applied to Co-based delafossites as the formation of the Co₃O₄ spinel structure has been also a challenge for, e.g., PdCoO₂^{7,8,10,11}. Our results suggest that the key to achieving the layer-by-layer growth of CuCrO₂ delafossite films is the nucleation of the structurally similar CuCr_{1-x}Al_xO₂ buffer layer at the interface when grown on structurally dissimilar substrates, e.g., conventional Al₂O₃ substrates. Thus, this discovery may provide a critical strategy for the epitaxial growth of other delafossites with the new CuCr_{1-x}Al_xO₂ buffer layer to accelerate innovations in future electronic and spintronic quantum devices made from delafossites.

Methods

Thin film growth. High quality CuCrO₂ thin films were grown on *c*-plane Al₂O₃ substrates by PLD using a polycrystalline CuCrO₂ target. The polycrystalline CuCrO₂ is prepared by sintering the mixture of Cu₂O and Cr₂O₃ at 1,100 °C for 10 h in air. The obtained pure polycrystalline CuCrO₂ were pelletized and annealed at 800 °C. Before the thin film growth, commercially available Al₂O₃ (0001) substrates (CrysTec, Germany) were annealed at 1,100 °C for 1 h to achieve atomically flat surfaces with step-terrace structure. For the CuCrO₂ film growth, the growth conditions were widely varied ($T = 400\text{--}800$ °C, $P_{\text{O}_2} = 0.01\text{--}500$ mTorr), whereas the repetition rate and energy of the KrF excimer laser ($\lambda = 248$ nm) were fixed at 5 Hz and 1.5 J/cm², respectively. The best CuCrO₂ epitaxial thin films were obtained at optimal growth conditions of $T = 650$ °C, $P_{\text{O}_2} = 10$ mTorr. After the growth, the samples were cooled to room temperature in $P_{\text{O}_2} = 100$ Torr.

Characterization. The crystal structure was characterized by X-ray diffraction (XRD) using a four-circle high-resolution X-ray diffractometer (X'Pert Pro, PANalytical; Cu $K\alpha_1$ radiation), and the thickness of the film (*d*) was calibrated using X-ray reflectivity (XRR). The surface morphology measurements were made with atomic force microscopy (Veeco Dimension 3100). Cross-sectional TEM specimens were prepared using low-energy ion milling at LN₂ temperature after mechanical polishing. HAADF STEM measurements were performed on Nion UltraSTEM200 operated at 200 kV. The microscope is equipped with a cold field emission gun and a corrector of third- and fifth-order aberration for sub-Angstrom resolution. The convergence half-angle of 30 mrad was used and the inner angle of the HAADF STEM was approximately 65 mrad. To minimize the electron-irradiation damage during EELS mapping, EELS spectra were measured at 0.01 s collection time.

Estimation of the enthalpy of formation (ΔH_f) using ab-initio DFT calculations. Ab initio DFT calculations were performed using the Vienna ab initio simulation package (VASP) code³², and the enthalpy of compound formation is estimated using the fitted elemental-phase reference energies (FERE) method³¹. The Perdew–Burke–Ernzerhof plus Hubbard correction (PBE + U) was used for the exchange–correlation functional³³, in which the double-counting interactions were corrected using the full localized limit (FLL)³⁴. The Hubbard U parameter of 3 eV ($U = 3$ eV) is used for all transition metals except Cu for $U = 5$ eV following previous work³¹. A plane wave basis set at a cutoff energy of 600 eV was used to expand the electronic wave functions, and the valence electrons were described using the projector-augmented wave potentials. The Γ -centered $9 \times 9 \times 9$ Monkhorst–Pack K-point grid was used for sampling the Brillouin zone. Input structures are obtained from the Inorganic Crystal Structure Database (ICSD) and all cells and atomic positions in our calculations were relaxed with the force criteria of 0.01 eV/Å. In the FERE approach, the enthalpy of formation (ΔH_f) of a chemical compound $A_{n_1}B_{n_2} \dots$ is expressed by the following equation:

$$\Delta H_f(A_{n_1}B_{n_2} \dots) = E_{tot}^{DFT}(A_{n_1}B_{n_2} \dots) - \sum_i n_i \mu_i^{DFT} - \sum_i n_i \delta \mu_i^{FERE}$$

where E_{tot}^{DFT} is the total energy per formula unit of a given compound, μ_i^{DFT} are the total energies per atom of the elements in their elemental reference phase, and $\delta \mu_i^{FERE}$ are the FERE correction energies of the elements. The $\delta \mu_i^{FERE}$ for 50 chemical elements are tabulated in the paper describing the FERE approach³¹.

Received: 13 May 2020; Accepted: 17 June 2020

Published online: 09 July 2020

References

- Shannon, R. D., Rogers, D. B. & Prewitt, C. T. Chemistry of noble metal oxides. I. Syntheses and properties of ABO₂ delafossite compounds. *Inorg. Chem.* **10**, 713 (1971).
- Prewitt, C. T., Shannon, R. D. & Rogers, D. B. Chemistry of noble metal oxides. II. Crystal structures of platinum cobalt dioxide, palladium cobalt dioxide, copper iron dioxide, and silver iron dioxide. *Inorg. Chem.* **10**, 719 (1971).
- Rogers, D. B., Shannon, R. D., Prewitt, C. T. & Gillson, J. L. Chemistry of noble metal oxides. III. Electrical transport properties and crystal chemistry of ABO₂ compounds with the delafossite structure. *Inorg. Chem.* **10**, 723 (1971).
- Mackenzie, A. P. The properties of ultrapure delafossite metals. *Rep. Prog. Phys.* **80**, 032501 (2017).
- Hicks, C. W. *et al.* Quantum oscillations and high carrier mobility in the delafossite PdCoO₂. *Phys. Rev. Lett.* **109**, 116401 (2012).
- Sunko, V. *et al.* Maximal Rashba-like spin splitting via kinetic-energy-coupled inversion-symmetry breaking. *Nature* **549**, 492 (2017).

7. Harada, T., Fujiwara, K. & Tsukazaki, A. Highly conductive PdCoO₂ ultrathin films for transparent electrodes. *APL Mater.* **6**, 046107 (2018).
8. Yordanov, P. *et al.* Large thermopower anisotropy in PdCoO₂ thin films. *Phys. Rev. Mater.* **3**, 085403 (2019).
9. Ok, J. M. *et al.* Pulsed-laser epitaxy of metallic delafossite PdCrO₂ films. *APL Mater.* **8**, 051104 (2020).
10. Brahlek, M. *et al.* Growth of metallic delafossite PdCoO₂ by molecular beam epitaxy. *Phys. Rev. Mater.* **3**, 093401 (2019).
11. Sun, J. X. *et al.* Growth of PdCoO₂ by ozone-assisted molecular-beam epitaxy. *APL Mater.* **7**, 121112 (2019).
12. Han, M. J. *et al.* Electronic transition and electrical transport properties of delafossite CuCr_{1-x}Mg_xO₂ (0 ≤ x ≤ 12%) films prepared by the sol-gel method: a composition dependence study. *J. Appl. Phys.* **114**, 163526 (2013).
13. Nie, S. B. *et al.* Solution-processed ternary p-type CuCrO₂ semiconductor thin films and their application in transistors. *J. Mater. Chem. C* **6**, 1393 (2018).
14. Shin, D., Foord, J. S., Egdell, R. G. & Walsh, A. Electronic structure of CuCrO₂ thin films grown on Al₂O₃(001) by oxygen plasma assisted molecular beam epitaxy. *J. Appl. Phys.* **112**, 113718 (2012).
15. Li, D. *et al.* Electrical, optical and structural properties of CuCrO₂ films prepared by pulsed laser deposition. *J. Phys. D: Appl. Phys.* **40**, 4910 (2007).
16. Lin, F., Gao, C., Zhou, X., Shi, W. & Liu, A. Magnetic, electrical and optical properties of p-type Fe-doped CuCrO₂ semiconductor thin films. *J. Alloy. Compd.* **581**, 502 (2013).
17. Sinnarasa, I., Thimont, Y., Presmanes, L., Barnabe, A. & Tailhades, P. Thermoelectric and transport properties of delafossite CuCrO₂:Mg thin films prepared by RF magnetron sputtering. *Nanomaterials (Basel)* **7**, 157 (2017).
18. Tripathi, T. S. & Karppinen, M. Structural optical and electrical transport properties of ALD-fabricated CuCrO₂ films. *Phys. Procedia* **75**, 488 (2015).
19. Lu, P., Xiong, J., Van Benthem, M. & Jia, Q. Atomic-scale chemical quantification of oxide interfaces using energy-dispersive X-ray spectroscopy. *Appl. Phys. Lett.* **102**, 173111 (2013).
20. Spurgeon, S. R., Du, Y. & Chambers, S. A. Measurement error in atomic-scale scanning transmission electron microscopy—energy-dispersive X-ray spectroscopy (STEM-EDS) mapping of a model oxide interface. *Microsc. Microanal.* **23**, 513 (2017).
21. Wang, P., D'Alfonso, A., Findlay, S., Allen, L. & Bleloch, A. Contrast reversal in atomic-resolution chemical mapping. *Phys. Rev. Lett.* **101**, 236102 (2008).
22. Forbes, B. *et al.* Contribution of thermally scattered electrons to atomic resolution elemental maps. *Phys. Rev. B* **86**, 024108 (2012).
23. Lee, H. N., Ambrose Seo, S. S., Choi, W. S. & Rouleau, C. M. Growth control of oxygen stoichiometry in homoepitaxial SrTiO₃ films by pulsed laser epitaxy in high vacuum. *Sci. Rep.* **6**, 19941 (2016).
24. Choi, W. S. *et al.* Atomic layer engineering of perovskite oxides for chemically sharp heterointerfaces. *Adv. Mater.* **24**, 6423 (2012).
25. Daulton, T. L. & Little, B. J. Determination of chromium valence over the range Cr(0)–Cr(VI) by electron energy loss spectroscopy. *Ultramicroscopy* **106**, 561 (2006).
26. Singh, S. B. *et al.* Correlation between p-type conductivity and electronic structure of Cr-deficient CuCr_{1-x}O₂ (x = 0–0.1). *Phys. Rev. B* **86**, 241103 (2012).
27. De Groot, F. *et al.* Oxygen 1s X-ray-absorption edges of transition-metal oxides. *Phys. Rev. B* **40**, 5715 (1989).
28. De Groot, F. Multiplet effects in X-ray spectroscopy. *Coord. Chem. Rev.* **249**, 31 (2005).
29. Jo, J. *et al.* Effects of the heterointerface on the growth characteristics of a brownmillerite SrFeO_{2.5} thin film grown on SrRuO₃ and SrTiO₃ perovskites. *Sci. Rep.* **10**, 3807 (2020).
30. Aston, D. *et al.* High-resolution X-ray spectroscopic study of the electronic structure of the prototypical p-type transparent conducting oxide CuAlO₂. *Phys. Rev. B* **72**, 195115 (2005).
31. Stevanović, V., Lany, S., Zhang, X. & Zunger, A. Correcting density functional theory for accurate predictions of compound enthalpies of formation: fitted elemental-phase reference energies. *Phys. Rev. B* **85**, 115104 (2012).
32. Kresse, G. & Furthmüller, J. Efficient iterative schemes for ab initio total-energy calculations using a plane-wave basis set. *Phys. Rev. B* **54**, 11169 (1996).
33. Perdew, J. P., Burke, K. & Ernzerhof, M. Generalized gradient approximation made simple. *Phys. Rev. Lett.* **77**, 3865 (1996).
34. Dudarev, S., Botton, G., Savrasov, S., Humphreys, C. & Sutton, A. Electron-energy-loss spectra and the structural stability of nickel oxide: an LSDA+U study. *Phys. Rev. B* **57**, 1505 (1998).

Acknowledgements

This work was supported by the U.S. Department of Energy, Office of Science, Basic Energy Sciences, Materials Sciences and Engineering Division (synthesis and microscopy) and the Computational Materials Sciences Program (theory). This research used resources of the National Energy Research Scientific Computing Center (NERSC), a U.S. Department of Energy Office of Science User Facility operated under Contract No. DE-AC02-05CH11231.

Author contributions

J.M.O., S.Y. and H.N.L. designed the experiment and wrote the manuscript with input from all authors. J.M.O. and H.N.L. grew films and conducted characterization. S.Y., A.R.L. and M.F.C. conducted STEM/EELS experiments. S.Y. and P.G. performed DFT calculation. All authors have given approval to the final version of the manuscript. J.M.O. and S. Y. contributed equally to this work.

Competing interests

The authors declare no competing interests.

Additional information

Supplementary information is available for this paper at <https://doi.org/10.1038/s41598-020-68275-w>.

Correspondence and requests for materials should be addressed to H.N.L.

Reprints and permissions information is available at www.nature.com/reprints.

Publisher's note Springer Nature remains neutral with regard to jurisdictional claims in published maps and institutional affiliations.



Open Access This article is licensed under a Creative Commons Attribution 4.0 International License, which permits use, sharing, adaptation, distribution and reproduction in any medium or format, as long as you give appropriate credit to the original author(s) and the source, provide a link to the Creative Commons license, and indicate if changes were made. The images or other third party material in this article are included in the article's Creative Commons license, unless indicated otherwise in a credit line to the material. If material is not included in the article's Creative Commons license and your intended use is not permitted by statutory regulation or exceeds the permitted use, you will need to obtain permission directly from the copyright holder. To view a copy of this license, visit <http://creativecommons.org/licenses/by/4.0/>.

This is a U.S. Government work and not under copyright protection in the US; foreign copyright protection may apply 2020, corrected publication 2023